Additive Manufacturing 94 (2024) 104505

Contents lists available at ScienceDirect

Additive Manufacturing

journal homepage: www.elsevier.com/locate/addma

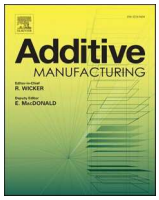

Operando visualization of porous metal additive manufacturing with foaming agents through high-speed x-ray imaging

Chenxi Tian [a], Jenniffer Bustillos [a], Akane Wakai [a], Ashlee Gabourel [a], Samuel J. Clark [b], Kamel Fezzaa [b], Atieh Moridi [a,*,1]

[a] Department of Mechanical and Aerospace Engineering, Cornell University, Ithaca, NY 14853, USA
[b] X-ray Science Division, Advanced Photon Source, Argonne National Laboratory, Lemont, IL 60439, USA

ARTICLE INFO

Keywords:
Porous metal
Metal foam
In-situ high-speed imaging
Synchrotron
Powder bed fusion

ABSTRACT

Porous metals find extensive applications in soundproofing, filtration, catalysis, and energy-absorbing structures, thanks to their unique internal pore structure and high specific strength. In recent years, there has been an increasing interest in fabricating porous metals using additive manufacturing (AM), leveraging its unique advantages, including improved design freedom, spatial material control, and cost-effective small-batch production. In this study, we conducted pioneering operando visualization of AM porous metal using a laser powder bed fusion (L-PBF) setup combined with a high-speed synchrotron x-ray imaging system. Single track printing experiments using Ti6Al4V (Ti64) combined with titanium hydride (TiH_2) and sodium carbonate (Na_2CO_3) as foaming agents, with varying mixing ratios were performed under different processing conditions. The results elucidate the dynamic development of porosity formation. The average pore size is significantly influenced by the particle size of foaming agents when pore coalescence is absent. For all foaming agent content tested in the current study, the number of pores is found to be more sensitive to changes in laser power than in laser scanning speed. Increasing linear energy density (increasing laser power or reducing laser scanning speed) promotes the foaming agent activation thereby porosity formation. However, high linear energy density skews pore distribution towards the surface despite forming deeper melt pools. In addition, the impact of additional factors including foaming agent's laser absorptivity and decomposition kinetics with respect to AM time scales should be carefully considered to avoid ineffective activation of foaming agents during the AM of porous metals.

1. Introduction

Porous metals or metal foams are a class of materials characterized by their unique internal structures, which consists of intentional pores or cavity inclusions. This distinctive architecture imparts interesting properties to porous metals such as low density, high strength-to-weight ratio, excellent energy absorption, and superior thermal and acoustic insulation capabilities [1]. Porous metal structures can be classified into two categories: open-cell structures, where pores are interconnected and closed-cell structures, where pores remain isolated. The fluid permeability enabled by inter-connected pores in open-cell porous metal structures gives rise to applications such as orthopedics, soundproofing, filtration, and catalysis [2–5]. On the other hand, closed-cell porous metal structures have excellent energy absorption performance while reducing weight and improving machinability compared to solid metal materials. This makes closed-cell type porous metal materials particularly suitable for structural use in industries like the automobile and aerospace [6–8].

Various conventional methods exist for fabricating porous metal materials. These include injecting gas into molten metal or introducing a foaming agent into molten metal during cooling [9–13]. Additionally, the directional cooling approach is employed as another method for fabricating porous metals in molten state yielding directional pores. Furthermore, the space holder method involves the use of a molds and sacrificial media to create casted porous metal structures [14–17]. In addition, solid-state techniques are also used in the conventional fabrication of porous metal material, namely sintering or powder metallurgy. Incomplete sintering of metal powder leaves cavities between partially fused powder particles, or foaming agents can be introduced to the metal powder to create porosity during the complete sintering [18–20]. These

* Corresponding author.
E-mail address: moridi@cornell.edu (A. Moridi).
[1] 124 Hoy Rd, Upson Hall Room 469, Ithaca, NY 14850, USA

https://doi.org/10.1016/j.addma.2024.104505
Received 2 April 2024; Received in revised form 2 October 2024; Accepted 19 October 2024
Available online 21 October 2024

aforementioned conventional methods are suitable for mass production of metal foam stocks. However, they have inherent limitations in the shape and size of the produced material stock/structures, as well as the minimum production quantity due to the need for expensive molds. Moreover, achieving spatial control over the pore size and distribution is challenging with these conventional porous metal manufacturing methods.

Additive manufacturing (AM) forms net-shaped components without the need for molds, enabling much smaller batch production compared to conventional methods, while having localized, highly dynamic thermal cycles [21]. These attributes enable AM to emerge as a new method of porous metal manufacturing. Broad application of AM in creating porous metal structures initially began in the field of orthopedic implants, where the economical low-volume production of AM enables patient-specific solutions [22]. The open-cell porous metal implants produced with AM allow for improved bone ingrowth and fluid permeability [23,24]. In addition, the fluid permeability of porous structures has also encouraged adoption of AM in fabricating open-cell porous metal parts for electrochemical applications such as catalysis [25–27]. While the aforementioned applications are great examples of the rapid development of AM open-cell porous metal structures, the development of AM closed-cell porous metal material is not on the matching level yet. AM of closed-cell porous metal employs feedstock metal powder that contains foaming agent. The mixed-in foaming agents decompose upon localized heating to create trapped gas pores in the printed structure due to the high cooling rate in AM. Some studies have shown success in producing closed-cell porous metal structures using both direct energy deposition (DED) and powder bed fusion (PBF) AM methods [28–33]. These studies show promising results that focus on mechanical performance and achieving high overall porosity levels. However, the characterization methods employed in the studies are limited to post-mortem methods, thereby overlooking the dynamic process of pore formation.

In the current study, we intend to explore the unchartered territory of operando monitoring of the metal foaming process in AM by leveraging the high-speed x-ray imaging capability at beamline 32-ID in Advanced Photon Source (APS), Argonne National Laboratory (ANL) [34,35]. The AM setup established at APS beamline 32-ID enables us to study the L-PBF process in situ using high-flux high-energy x-rays. We chose Ti6Al4V (Ti64) as the base metal for porous metal printing. Titanium has a high strength-to-weight ratio and corrosion resistance, making it a prime candidate for use in aerospace, marine, and automobile industries, while its high melting point poses great difficulty for conventional porous metal fabrication methods. We combined Ti64 with TiH_2 and Na_2CO_3 foaming agents at different mixing ratios to systematically study how different foaming agent content, laser power, and laser scanning speed impact the pore size and overall porosity level. Other factors including pore count and pore depth were also analyzed. The results from this operando study will provide insight into designing feedstock and processing conditions for manufacturing metal foams with desired porosity characteristics.

2. Method and materials

2.1. Single track printing and high-speed X-ray imaging

A mixed powder of Ti6Al4V (Ti64) and foaming agents were used as feedstock for printing porous metal. Foaming agents used in the pilot study included TiH_2 and Na_2CO_3, while only Na_2CO_3 was used in further systematic studies due to the lack of pores observed in TiH_2 pilot studies. The size ranges of powder were 15–45 μm for Ti64, 37–53 μm for TiH_2, and 37–53 μm for Na_2CO_3, respectively. While Ti64 and TiH2 were purchased off the shelf from Carpenter Additive and Thermo Scientific directly within the desired range, Na_2CO_3 powder was produced in-house from 30-minute ball milling of anhydrous Na_2CO_3 solids with stainless steel media. The foaming agent particle size was chosen to keep the particle size of all constituents in the feedstock in line with the typical L-PBF feedstock size range. The sieving process in the production of Na_2CO_3 powder in-house limited the minimum size of the foaming agent particle to 400 mesh or 38 μm. This also reduced foaming agent agglomeration, which could be problematic given the irregular morphology of the Na_2CO_3 particles after ball milling. For the pilot study, 5 wt% and 10 wt% mixing ratios were both used for TiH_2 and Na_2CO_3. Feedstock with 1 wt%, 3 wt%, and 5 wt% of Na_2CO_3 were used in the subsequent systematic study due to similar foaming performance shown in the pilot study using 5 wt% and 10 wt% foaming agents. All mixed powder feedstock was mechanically mixed before transportation and manually agitated before use due to the agglomeration tendency of Na_2CO_3 powder.

Single track printing of porous metal was performed at ANL APS beamline 32-ID, which enabled continuous in-situ high-speed x-ray imaging at the frame rate of 50 kHz. The experimental setup is schematically shown in Fig. 1.

The X-ray beams used in all experiments were white beam with the first harmonic energy of 24.4 keV for maximum phase contrast. The imaging frame size of 1024 ×400 pixels was used to capture laser line scans of 1.6 mm in length. An IPG continuous-wave ytterbium laser with a wavelength of 1070 nm was used as the energy source in the powder bed fusion process, and the laser spot size was 45 μm at the focal plane (experiments were performed with 2.32 mm offset from the focal plane to achieve adequate spot size). As shown in Fig. 1(a), the unfused sample was placed on a 3-axis motorized stage (not shown in the schematic), with the region of interest (top portion of the substrate with powder) in the x-ray path. The laser fusion process was carried out in a vacuum-purged and argon-backfilled chamber. Visible light imaging was performed using a Photron FastCam SA-Z high-speed camera with a 100 μm LuAg:Ce scintillator that converted X-rays to visible light. The combination of 1024 pixel by 400 pixel frame size, 50 kHz acquisition rate, and 1 μs exposure time was chosen to capture the entire line scan from laser firing to complete material fusion. In this configuration, the resolution of acquired images was 2 microns/pixel. The powder bed (the unfused sample) assembly is shown schematically in Fig. 1(b). Two glassy carbon strips constrained the 400 μm thickness commercially pure titanium substrate in a sandwich structure to allow x-ray transparency while holding the powder bed on top of the substrate. A defocused laser beam with a 95 μm spot size at various power levels (300, 350, 400, and 450 W) was directed to the top surface of the powder and scans along the centerline of the powder bed at various speeds (500, 600, 700, 800, and 1100 mm/s). Further details regarding the choice of processing parameters are discussed in Section 3.1.

2.2. X-ray radiograph postprocessing

Given the stochastic nature of porosity forming in porous metal printing and the large dataset size produced from the systematic study, an automated framework for porosity and melt pool detection was necessary. Such a framework was created using the combination of ImageJ and Python to maintain consistency in data analysis and allow comparison between experiments performed under different processing conditions. A simplified diagram of the developed framework is shown as a flowchart in Fig. 2(a). Processing of the image sequence from each experiment started with background feature removal via division of the first 50 frames average on all frames. The image sequence was converted to an 8-bit format to facilitate further denoising and porosity detection in later steps. All image sequences were truncated to 250 frames with 1024 pixel by 150 pixel frame size to reduce computation load while fully capturing the dynamics in the melt pool below the powder substrate interface. Due to the size difference between the laser spot (95 μm) and thickness of substrate used (400 μm, limited to manufacturing capability), some unfused feedstock particles remained above the substrate after laser scanning. The portion of the frame above the powder substrate interface was thus excluded from the porosity

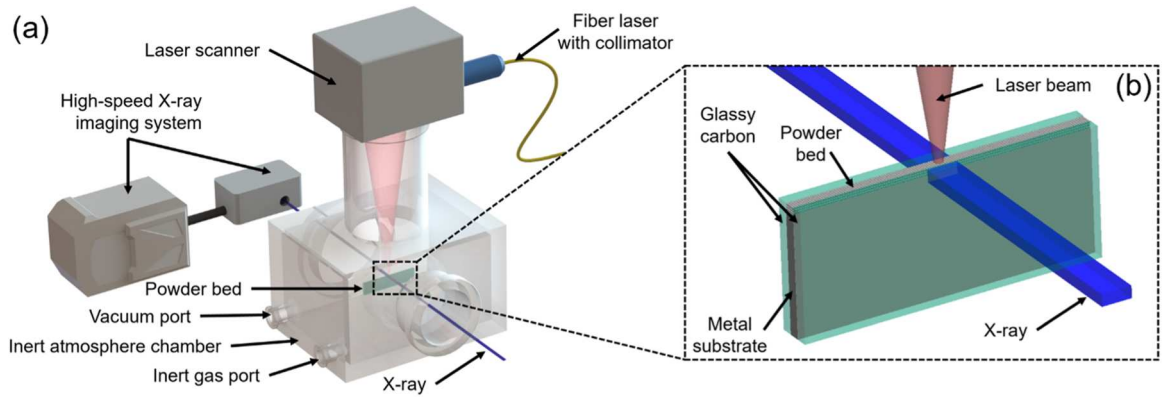

Fig. 1. (a) Schematic showing the experimental set-up for in-situ L-PBF high-speed x-ray imaging. The L-PBF single track printing is performed in an inert atmosphere chamber refilled with argon gas after vacuum purging. The powder bed (un-melted sample) is mounted on a motion stage to position the printing region on the X-ray beam path. The laser beam comes from the top of the chamber and is aimed with a galvanometer scanning system and the high-speed imaging system is positioned downstream of the powder bed on the x-ray beam path. (b) Detailed schematic of the powder bed assembly. A sandwich structure of a pair of glassy carbon (x-ray transparent) sidewalls and a thin metal substrate is used to create the powder bed. The height of the powder bed is determined by the height difference between glassy carbon and substrate and the powder is spread manually with a flat scraper.

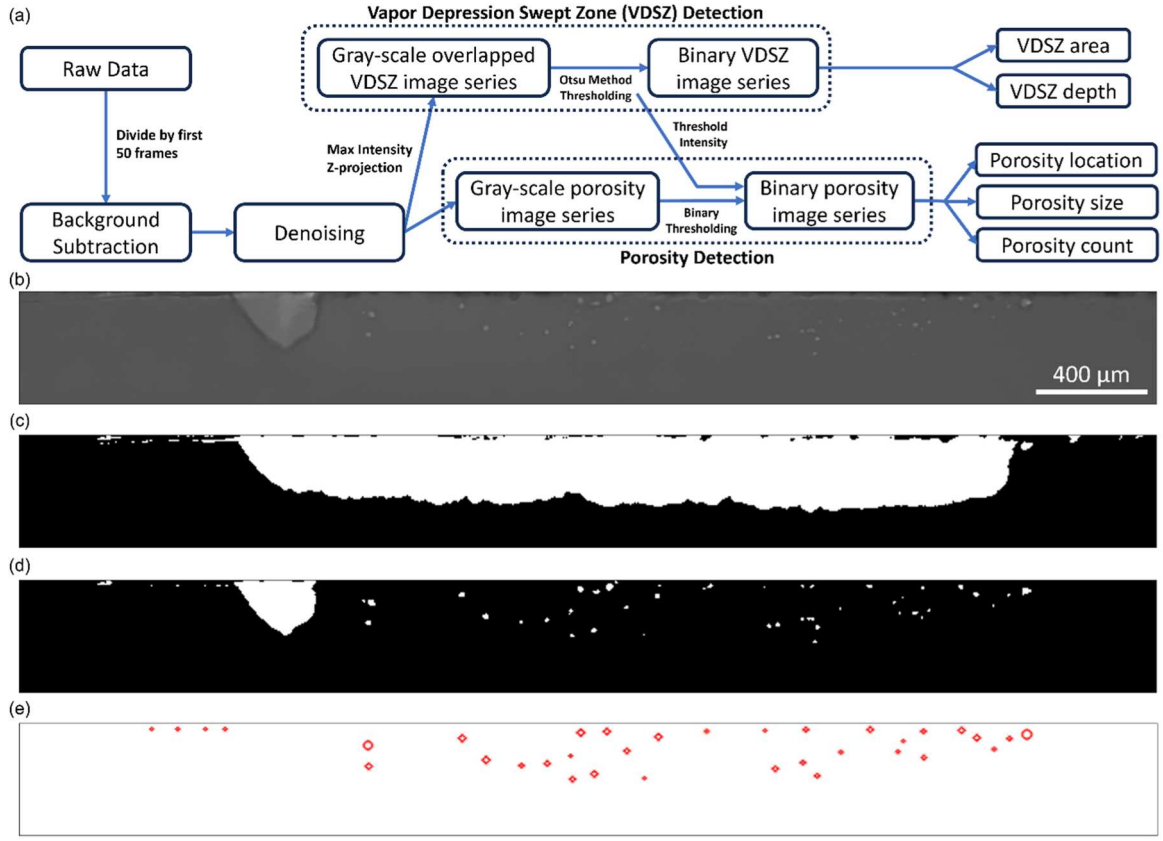

Fig. 2. (a) Flow chart showing the key steps taken to post-process the image sequence and the acquired outputs used in subsequent data analysis. Sample images (cropped in height to improve readability) of (b) after background subtraction and denoising, (c) after thresholding in vapor depression swept zone detection, (d) after thresholding in porosity detection, (e) after pore size and location marked using equivalent-area circles.

analysis given no distinguishable contrast was present between pores and un-melted feedstock particles.

While the homogeneous substrate in theory should provide a clean background for porosity detection, the noise present in the actual data proved further denoising to be essential for robust porosity detection with minimized errors. To combat this issue, all images were processed through the OpenCV fastNlMeansDenoising function, which is a fast image-denoising package in Python that uses the Non-local Means Denoising algorithm [36]. One sample image after denoising is shown in Fig. 2(b). Furthermore, the lack of contrast around the melt pool boundary prohibited direct detection of the melt pool perimeter. However, there is typically a monotonic correlation between the depth of the vapor depression and the depth of the melt pool. This means that for the same material system, a deeper vapor depression typically indicates a deeper melt pool, and vice versa [37,38]. Therefore, the sum of all vapor depressions in previous frames was considered the vapor depression

swept zone (VDSZ), providing a close 2D approximation of the volume of metal that has undergone melting and solidification. The area of VDSZ was used as a reference to normalize the pore population, as detailed in Section 3.4. Additionally, the morphology of the vapor depression, especially its depth, serves as a good indicator of the energy density of the laser [39,40]. Thus, the depth of the stable portion of VDSZ was used as the reference to normalize the average pore depth, creating a metric to approximate the vertical spread of pores within the meltpool, as detailed in Section 3.5. All image sequences were converted into stacked images with frame numbers corresponding to image numbers. Max Intensity projection selects pixels of the highest intensity from every image throughout a stack to construct a single 2D image. It was used in every frame/image to obtain the sum of vapor depressions from all previous frames. The Otsu method was subsequently used to identify the optimal intensity value for binary thresholding to mitigate the slight intensity variation present across image sequences from different experiments. A sample image showing VDSZ in binary format is shown in Fig. 2(c). VDSZ area and depth for each frame of the experiment were obtained respectively through bright pixel counting and averaging the bottom edge y-coordinate of VDSZ in the stable region. Since the small number of pores in the frame caused erroneous binary thresholding from using the Otsu method directly on denoised images, the optimal intensity value for binary thresholding images in VDSZ detection was used instead. One sample resultant binary image for porosity detection is shown in Fig. 2(d). The optimal thresholding intensity was determined on a frame-by-frame basis to minimize the impact of variation in overall pixel intensity across frames from the same experiment. The resultant binary images for porosity detection were labeled using the OpenCV SimpleBlobDetector function as shown in Fig. 2(e) while the porosity location and size (diameter of the area-equivalent circle) were saved in lists for each frame [36].

It is important to point out that the porosity detection criteria included a filter to exclude artifacts in the image after thresholding. These artifacts include long patches of bright pixels caused by occasional non-parallel substrate top surface, powder particles slipping between the glassy carbon side support and substrate, etc. This filter only allows detection as the porosity of a bright pixel cluster whose area is less than 500 pixel^2 or 2000 μm^2, circularity is more than 0.1, convexity is more than 0.8, and inertia ratio is more than 0.5. In addition to the aforementioned efforts to minimize noise in the raw data during pore detection- including denoising to remove global noisy pixels and Otsu thresholding to separate pore-generated high-intensity signals from the background- a minimum detection limit of 2 pixels (an area of 4 pixel^2) is also enforced in the SimpleBlobDetector. Despite these efforts to reduce noise, the experimental setup resolution limit of 2 μm/pixel still causes uncertainty in the detection of small pore, which should be considered when interpreting the results in the later sections. On top of the stringent detection process for each frame in the image sequence obtained, a Savitzky Golay filter with a window size of 51 frames and polynomial order of 4 was also employed in plotting the porosity count development over time (frames) to resolve the fluctuation caused by the minor flickering of global pixel intensity in image sequences. All confidence intervals and errors shown in figures in Section 3 were calculated from three repeated experiments of each feedstock and processing parameter combination.

3. Results and discussion

The results and discussions are organized in the following sections: we start from a pilot study (Section 3.1) with different foaming agents and choose to proceed with Na2CO3 for further investigations. Different pore characteristics including pore motion (Section 3.2), size (Section 3.3), count (Section 3.4), and depth (Section 3.5) are discussed. Finally, ways to control overall porosity levels and insights into the impact of foaming agent laser absorptivity are presented in Section 3.5 as well.

3.1. Pilot study

A pilot study to verify the feasibility of single track printing of porous metal was conducted to narrow down the processing parameters, foaming agent composition, and mixing ratio applicable to high-speed imaging experiments before conducting our systematic study. The processing parameters were chosen from combinations of power in the range of 150 – 400 W and scanning speed in the range of 400 – 1100 mm/s. The processing conditions tested span across lack of fusion mode, conduction mode, and stable and unstable keyhole modes. The preliminary foaming agent choices were Na_2CO_3 and TiH_2, whose thermal decomposition reactions are shown below:

$$TiH_2\ (s) \rightarrow Ti\ (s) + H_2\ (g)$$

$$Na_2CO_3\ (s) \rightarrow Na_2O\ (s) + CO_2\ (g)$$

The gaseous thermal decomposition products from these foaming agents create gas porosity in the Ti64 base metal, while the non-gaseous byproduct of the decomposition remains in the base metal. The Ti released from TiH2 decomposition has only a minor influence on the chemical composition of theTi64 base metal. Additionally, Ti alloys have demonstrated excellent resistance to unlikely corrosive reactions with Na_2O, the byproduct of Na_2CO_3 decomposition. The further breakdown of Na_2O into sodium vapor and oxygen requires very specific control of temperature and partial vapor pressure of sodium that are not present in AM [41]. Moreover, TiH_2 and Na_2CO_3 are typical carbonate and hydride used in conventional metal foaming and have shown feasibility in AM foaming of Ti alloy in pioneer experimental studies using DED and L-PBF methods [42,43]. The impact of solid Na₂O on the microstructure and mechanical properties of these porous structures is beyond the scope of the current work but warrants further investigation.

The obtained image sequences from the pilot study were processed using the ImageJ Over/Under thresholding function to highlight the formation of pores under the powder substrate interface. One signature frame each from 10 wt% Na_2CO_3 and TiH_2 experiments under different processing conditions is shown in Fig. 3.

In conduction mode, which was indicated by the minimal vapor depressions shown in Fig. 3(a)(b), no porosities were present below the powder/substrate interface for both Na_2CO_3 and TiH_2 experiments. While this shows lower porosity content in conduction mode, it does not necessarily indicate a complete lack of pore formation, as our experimental setup only captures pore formation below the powder substrate interface. However, the feasibility of this experimental setup to capture the formation of pores and overall porosity level development was verified since porosities were present in experiments under keyhole mode processing conditions, as shown in Fig. 3(c)-(e). Moderate amounts of pore formation under both stable and unstable keyhole modes were observed in experiments using feedstock powder mix with 10 wt% Na_2CO_3 as shown in Fig. 3(c)(e). While the higher energy density in the unstable keyhole mode gave rise to foaming agent activation, it also introduced keyhole pores at the bottom of the melt pool. These pores have more irregular morphology when compared with the mostly circular porosities produced by foaming agent particles, which are more uniformly distributed in the upper portion of the melt pool.

On the other hand, minimal to no pores were present in the experiments using feedstock powder mix with 10 wt% TiH_2, as shown in Fig. 3 (d)(f) for stable keyhole mode and unstable keyhole mode, respectively. This was surprising given that TiH_2 is a widely used foaming agent in metal foam productions with conventional manufacturing methods such as powder metallurgy and casting [44]. However, much more localized heating in AM compared to conventional methods and the foaming agent decomposition temperatures are not to be overlooked. The decomposition of TiH_2 is reported to become significant at about 450 °C, and the hydrogen desorption kinetics is much faster when the temperature is above 500 °C [45]. We hypothesize that the drastic difference between TiH_2 decomposition temperature and Ti64 melting

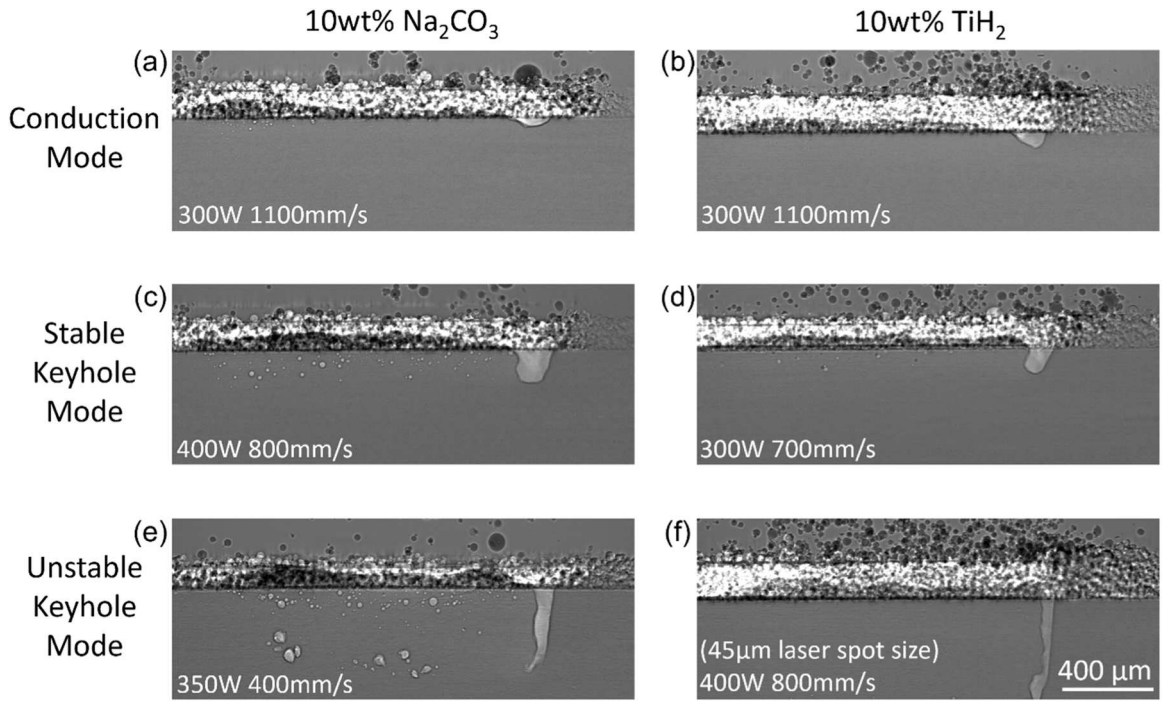

Fig. 3. Sample image showing foaming results in experiment using the following foaming agent and processing conditions respectively: (a) 10 wt% Na_2CO_3, conduction mode; (c) 10 wt% Na_2CO_3, stable keyhole mode; (e) 10 wt% Na_2CO_3, unstable keyhole mode; (b) 10 wt% TiH_2, conduction mode; (d) 10 wt% TiH_2, stable keyhole mode; (f) 10 wt% TiH_2, unstable keyhole mode.

temperature caused a rapid and potentially premature hydrogen gas generation, with most of the gas escaping through the powder bed before entering the observable region of Ti64 melt pool below the powder-substrate interface. The high cooling rate in AM could be beneficial to freeze gas pores in place if hydrogen gas is released in the melt pool. However, the lack of thickening agents that are commonly used in conventional methods would render the viscosity of the melt pool in AM too low for stable foaming of certain agents [46].

As a result of the poor foaming performance of TiH_2 in our single-layer experimental setup, Na_2CO_3 was determined to be the foaming agent of choice for further systematic studies. The systematic studies included different process parameter sets to create control groups where only one processing parameter, such as laser power or scanning speed, is varied within the group. The processing parameter sets were all within the stable keyhole mode to make sure foaming porosities were captured in the region below the powder-substrate interface while avoiding the formation of uncontrolled keyhole porosities. No significant porosity level differences were present in the pilot study experiments using feedstock with 5 wt% and 10 wt% Na_2CO_3. Therefore, the range of feedstock Na_2CO_3 content was chosen to be 0 – 5 wt% to avoid potential foaming agent saturation. Feedstocks with 1, 3, and 5 wt% of Na_2CO_3 foaming agent mixed in were used in the systematic study to explore the impact of foaming agent content on the overall porosity formation.

3.2. Pore formation and motion

Two primary factors contribute to the source of internal pores in metal parts produced with AM: material-induced and process-induced [47,48]. Defective feedstock powder that carries internal pores is the material source of pores while the process-induced porosity is more complicated [49,50]. Process-induced porosity typically originates from an improper choice of processing parameters, with examples of lack-of-fusion pores caused by low energy density, and unstable keyhole pores caused by unstable vapor depression from excessive energy input [51]. These two types of pores have irregular morphology and can act as origins of internal microcracks when the material is under load. Operating in a stable keyhole regime can create spherical entrapped gas pores, although the occurrence is rare. Conventional keyhole pores either trap metal vapor from localized regions of high energy density to form pores near keyhole tip at the bottom of the meltpool or trap environment gas from the volatile melt pool top surface and thus creating pores near the top [52,53]. Decomposition of added foaming agent, on the other hand, provides a more controlled source of entrapped gas within the melt pool, to create pores with more uniform distribution within the meltpool, and to enable more intuitive pore characteristic control in the production of porous metal structures.

The pilot study has shown the feasibility of creating porous metal structures with the addition of thermally decomposing foaming agent. The comparison between Fig. 3 (c) and Fig. 3 (d) shows that adding a proper choice of foaming agent (Na_2CO_3) can introduce higher porosity level than just printing the base metal without foaming agents (or with improper foaming agent) using stable keyhole regime processing conditions. To further validate the application of foaming agent thermal decomposition in the manufacturing of porous metal using L-PBF, thermodynamic calculations were performed and detailed in **Supplementary Notes**. It is estimated that the thermal decomposition of the foaming agent ($\leq$ 5 wt%) completes within less than 10 μs, which is much shorter when compared to the laser dwelling time of overall 100 μs based on typical L-PBF scanning speed. Additionally, the thermal decomposition of the foaming agent ($\leq$ 5 wt%) accounts for less than 5 % of the energy by the feedstock powder from the laser emission. This validates the feasibility of adding a foaming agent to create entrapped gas pores for the manufacturing of porous metal using L-PBF despite its high laser scanning speed. The low energy use in the decomposition of foaming agents also minimizes alterations needed from the optimal L-PBF processing parameters of the base metal material.

In fact, with the image sequences captured at a 50 kHz frame rate in the current study, there is a 20 μs interval between each frame. No dynamic process of pore formation or individual pore size development was observed, consistent with the shorter estimated foaming agent decomposition time of less than 10 μs and the 20 μs interval between frames (calculations detailed in **Supplementary Note 1**). However, the

pore motions and their interactions with neighboring pores and the keyhole vapor depression are captured in the image sequences such as the one shown in Fig. 4(a). The in-plane motion of pores is shown through image sequence post-processing detailed in Supplementary Figure 1 and the trajectory of each pore is indicated by an arrow. These trajectories could provide some insights into the dynamics of the pores. Fig. 4(b) illustrates the regular pore motion patterns shown in most of the experiments in the current study, where fully developed pores are injected below the powder substrate interface in the melt pool, entering circulations within the melt pool or following flows along the top or bottom sides of the melt pool. This flow pattern agrees with the complex flow behavior observed in the keyhole mode L-PBF process, as experimentally demonstrated using a similar operando synchrotron setup as shown in Fig. 1 with only minor differences in material and imaging configuration [54]. Interestingly, it is also observed in the current study that oscillatory vaper depression size changes cause disturbance to the regular pore motion pattern. This phenomenon is illustrated in Fig. 4(c), where pore motion near the back wall of the vapor depression is shown to alter from circulation to attraction towards a low-pressure zone created by shrunk vapor depression size.

The attraction of pores towards the vapor depression during oscillatory vapor depression size change leads the way to one of the several ways pores escape from the melt pool. In fact, three pathways of pore elimination/escape are found in the current study and shown in Fig. 5. These include: (I) Escaping via vapor depression, which can be found in most experiments regardless of the presence of oscillatory vapor depression size changes; (II) Escaping via melt pool top surface; and (III) pore coalescence, which is very rare occurrence in all experiments and cause reduction in pore count. While the current study reveals the unique oscillatory motion of the pores and the pathways of pore escape in AM porous metal, the large region of interest and the resulting limited frame rate make a systematic quantitative analysis of pore trajectories infeasible. Accurate pore labelling and tracking require sufficiently small pore displacements between frames to reduce imaging obstruction and ambiguous tracking of neighboring pores of similar size. Future studies will need to employ a much higher frame rate, at the expense of region of interest size, to meet these requirements and enable a focused analysis of pore trajectories.

3.3. Pore size

Fig. 6 shows the dynamic development of average pore size and comparison of average pore size in the final state of experiments under various laser powers, laser scanning speeds, as well as different feedstock foaming agent contents. In post-processing of the obtained high-speed x-ray image sequences, the average pore size of each frame was calculated to represent the pore size statistics given the stochastic nature of pore formation. The average statistics of the last 50 frames in each experiment were calculated to represent the stabilized average pore size after complete melt pool solidification, and group averages with standard deviations were calculated from the three repeated experiments.

At the start of most experiments, the average pore size was the smallest, and it increased as laser scanning proceeded. The development of average pore size using 5 wt% foaming agent while holding laser powder constant or holding scanning speed constant is shown in Fig. 6 (a) and (c) respectively. We can see an increasing trend in average pore size in the initial transient stage in all experiments, which is likely due to heat accumulation. At the start of the single track laser scan, the substrate is at a relatively lower temperature. As the laser beam scans along the powder bed and fuses material, heat accumulates in the substrate, which is in the conductive cooling path of the melt pool. This contributes to a higher melt pool temperature since the substrate progressively heats up while the laser energy input remains constant. The higher melt pool temperature from heat accumulation helps activating foaming agent particles with larger diameter, which contributes to the formation of larger pores and the increase in average pore size. Furthermore, fluctuations in the pore size increase can be observed in both experiment groups, which confirms the stochastic nature of the pore formation process. Formation of a large pore at the beginning of the line scan can introduce a large fluctuation in the average pore size since the number of pores present is still small, while fewer fluctuations are present at the later stages of the line scan. The absence of significant shifts in average pore size after the laser turns off (indicated by dashed cutoff lines on curves) signifies the short timescale of pore size development and stable pore size during melt pool solidification.

As shown in Fig. 6(b) and (d), the impact of different laser power or scanning speed on the average pore size is very minor, with higher energy density processing conditions (high laser power or low scanning

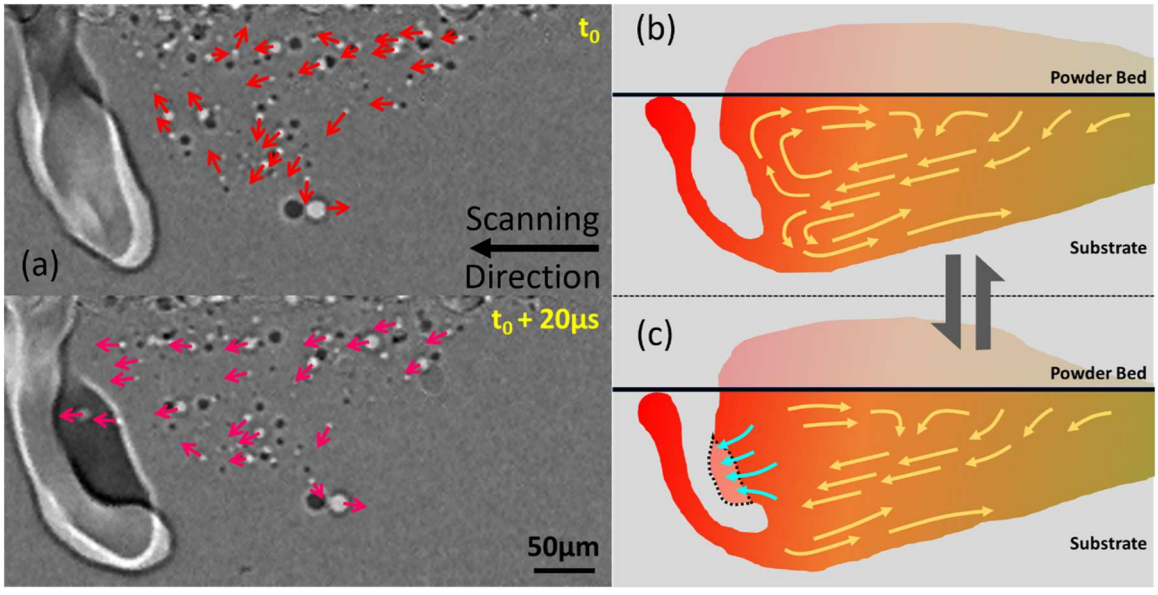

Fig. 4. (a) Image sequence showing pore motions during a vapor depression expansion and contraction. All directions of the in-plane motion of pores are indicated by the arrow on the X-ray image sequence after post-processing (detailed in Supplementary Figure 1). (b) Illustration of normal pore motion patterns in the melt pool (c) Pore attraction towards low-pressure zone during oscillatory vapor depression size change. Flow patterns in (b) and (c) depict pore motions observed in this study and are guided by previous work in the field [54].

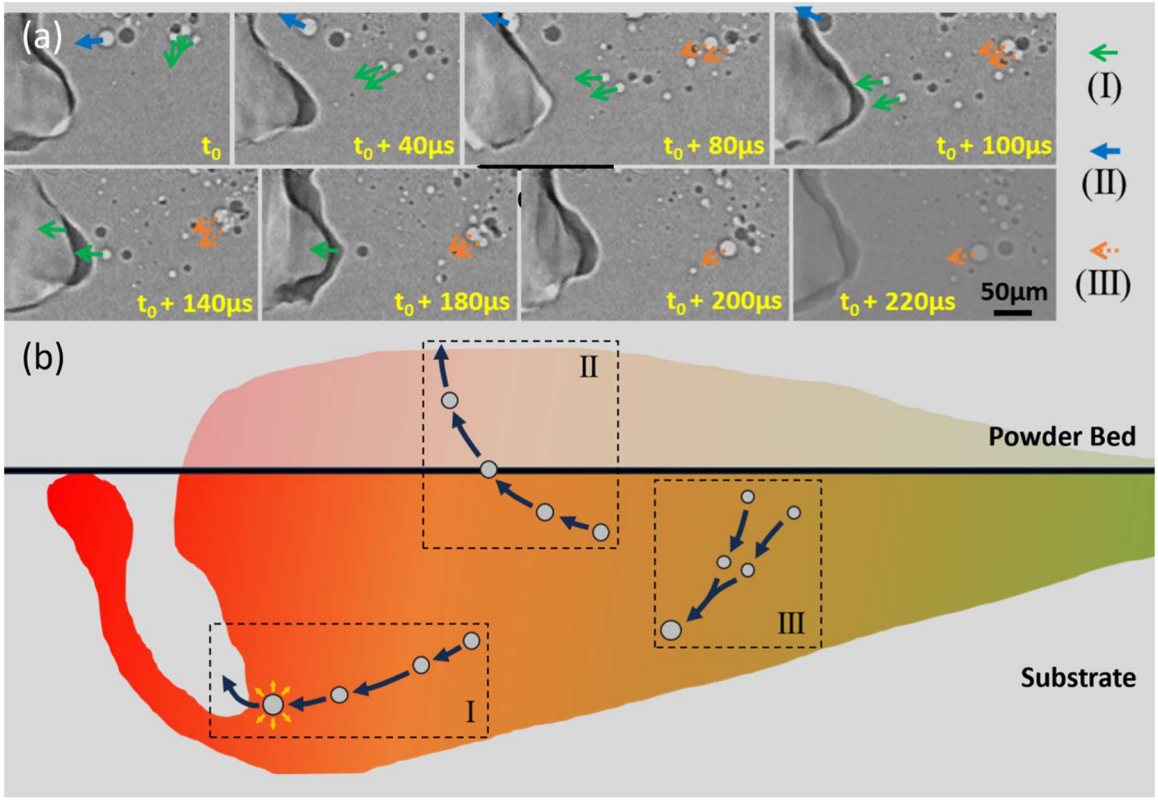

Fig. 5. (a) Image sequence showing different pathways of pore elimination during porous metal AM using L-PBF. All directions of the in-plane motion of pores are indicated by the arrow on the X-ray image sequence after post-processing (detailed in Supplementary Figure 1). (b) Illustration of different pore elimination pathways: (I) Escaping through vapor depression side wall; (II) Escaping through melt pool top surface; (III) Pore coalescence.

speed) producing slightly larger pores on average. Similarly, the different feedstock foaming agent content also showed minimal variation in stabilized average pore size, as shown in Fig. 7(a), despite the different energy densities (constant laser power, varying scanning speed) used.

To investigate other factors influencing pore size (besides processing parameters and foaming agent content), the size distribution of the foaming agent powder was obtained from ImageJ particle analysis on multiple scanning electron microscope (SEM) images of Na_2CO_3 powder (taken on a Tescan Mira Field Emission SEM). The size distribution of the foaming agent powder and all detected pores in our experiments are plotted together in Fig. 7(b). The matching distribution of pore size and foaming agent particle size suggests that each pore was likely formed from a single foaming agent particle (when pore coalescence is not present). This means foaming agent powder size may have a major influence on the size of the formed pores, which is in line with findings in metal foam production using conventional methods[55]. In addition, the distribution indicates a bias towards small pores, with the number of pores drastically reducing as pore diameter increases. These findings highlight the possibility of controlling the pore size in porous metal production using L-PBF using foaming agent particle size rather than processing conditions.

3.4. Pore count

While the pore size reflects the refinement of pores in AM porous metal, pore count could be a good indication of the likelihood of foaming agent decomposition. Given the matching size distribution of pores and foaming agent particles shown in Fig. 7(b) and the rare occurrence of pore coalescence observed in the current study, we hypothesize that the number of pores correlates to the number of decomposed foaming agent particles. The absolute pore count from each high-speed X-ray image frame was acquired through the framework detailed in Section 2.2, as shown in Fig. 8. In addition, the pore count statistics were normalized on a frame-by-frame basis with the area of the vapor depression swept zone to reflect the population density of pores as shown in Fig. 9.

When laser scanning speed was held constant, the increase in pore count all terminates after the laser is turned off (indicated by dashed cutoff lines on curves), as shown in Fig. 8(a). This indicates the insufficient temperature in the cooling melt pool to activate further Na_2CO_3 decomposition. Despite the outlier of 300 W, 800 mm/s runs, the stabilized average pore count shown in Fig. 8(b) indicates an increasing trend of the absolute number of pores formed with increasing laser power. Laser scanning speed did not show a significant impact on the rate of pore formation, indicated by the similar slope of all curves in Fig. 8(c). The stabilized average pore count of experiments using a 5 wt % foaming agent feedstock was insensitive to changing scanning speed in the range of 500–700 mm/s, as shown in Fig. 8(d). However, when the laser scanned too quickly, the energy density still remained within the processing window of Ti64, but inevitably led to a slight reduction in the melt pool temperature compared to that of runs with lower scanning speed. The reduced melt pool temperature could lower the heat transport to the foaming agent particles, thereby limiting the decomposition process via the rate of heat transfer rather than the decomposition rate, resulting in a much lower pore count in the stabilized state of 800 mm/s runs. More details on the activation of foaming agent thermal decomposition is provided in the latter part of Section 3.5. Unlike the 5 wt% foaming agent runs, the effect of scanning speed on pore count in the stabilized states was much more pronounced in the lower foaming agent content runs, as shown in Supplementary Figure 4(a) in appendix. This more reasonably aligns with the fact that variations in laser power and scanning speed both contribute to changes in energy density that is required to decompose the foaming agent. Under the same processing conditions, as shown in Supplementary Figure 4(a), the pore counts

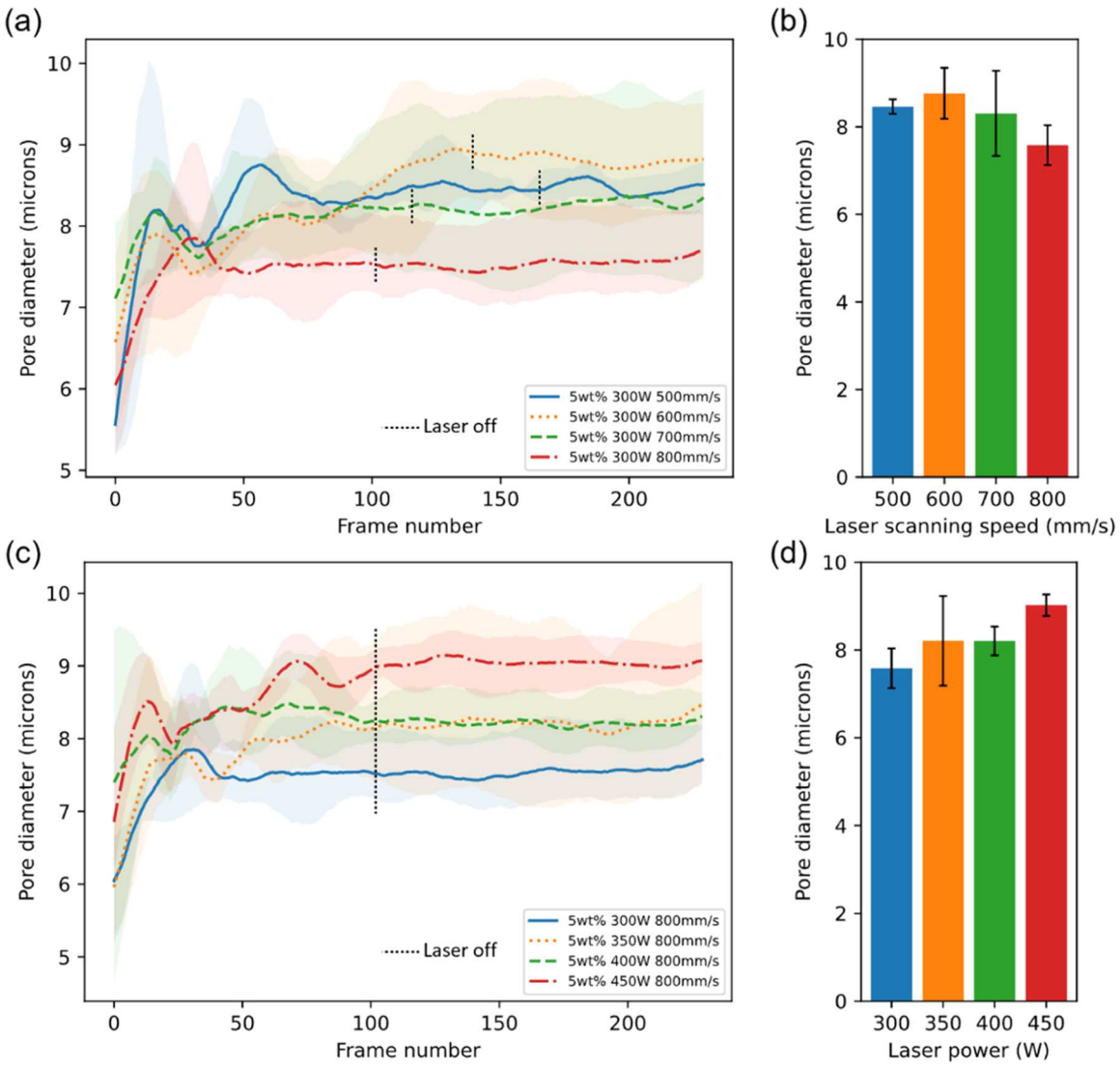

Fig. 6. (a) Average pore diameter development with respect to frame number of experiments using 5 wt% Na_2CO_3, 300 W laser power, and various laser scanning speeds. (b) Final average pore diameter of experiments using 5 wt% Na_2CO_3, 300 W laser power, and various laser scanning speeds. (c) Average pore diameter development with respect to frame number of experiments using 5 wt% Na_2CO_3, 800 mm/s laser scanning speed, and various laser powers. (d) Final average pore diameter of experiments using 5 wt% Na_2CO_3, 800 mm/s laser scanning speed, and various laser powers.

display inconclusive and non-monotonic relationships with the foaming agent contents in the range explored in the current study. This is likely due to the unusual foaming agent laser absorptivity, which is discussed in Section 3.5, along with the potential reasons for the limited variation seen in final pore count in 5 wt% foaming agent content.

Crowding of the pores is another important aspect not to be overlooked when discussing the number of pores. When too many pores are formed within a unit volume, the tendency for the pores to coalesce with each other increases due to Ostwald ripening. Although pore coalescence is rarely observed in the current study, it could lead to an increase in the individual porosity size and a reduction in pore count. This could potentially cause a deviation from the expected design when a metal foam with densely-populated refined pores is desired. Normalizing the absolute pore count with the area of the vapor depression swept zone could be considered a good approximation to the population density of pores. As shown in Fig. 9**(a)**, at the beginning of line scans, the melt pool gets to its most crowded state before the density of the pore population slowly reduces as the line scan proceeds and the melt pool enters a steadier state. This could be caused by the slight delay at the start as the actuated optics in the scanhead accelerate to reach the set scanning speed, during which the initial region in the melt pool could be unstable from higher than nominal energy input. Therefore, final values of normalized pore count towards the end of the line scans are the better representations of the steady-state pore population density. In contrast to the trend observed in the final absolute pore count, the lower scanning speed experiments (when laser powder is held constant) showed the lowest pore population density in Fig. 9(b), despite the higher number of pores present. It is also shown in Supplementary Figure 4(b) in appendix that this trend in normalized porosity count is present across different feedstock foaming agent content. We hypothesize that the increase in melt pool dimension under lower scanning speed overshadowing the increase in absolute porosity count is likely the main cause of these two contrary trends in porosity count.

3.5. *Pore Distribution and Overall Porosity Level*

The depths to which pores travel show a stochastic nature, with no significant correlation between the size of individual pores and the depth they reach. Therefore, an average normalized pore depth was calculated for the final state of each experiment control group to reflect the vertical distribution of pores. Fig. 10(a) illustrates the definition of average pore depth D_p and average vapor depression swept zone depth

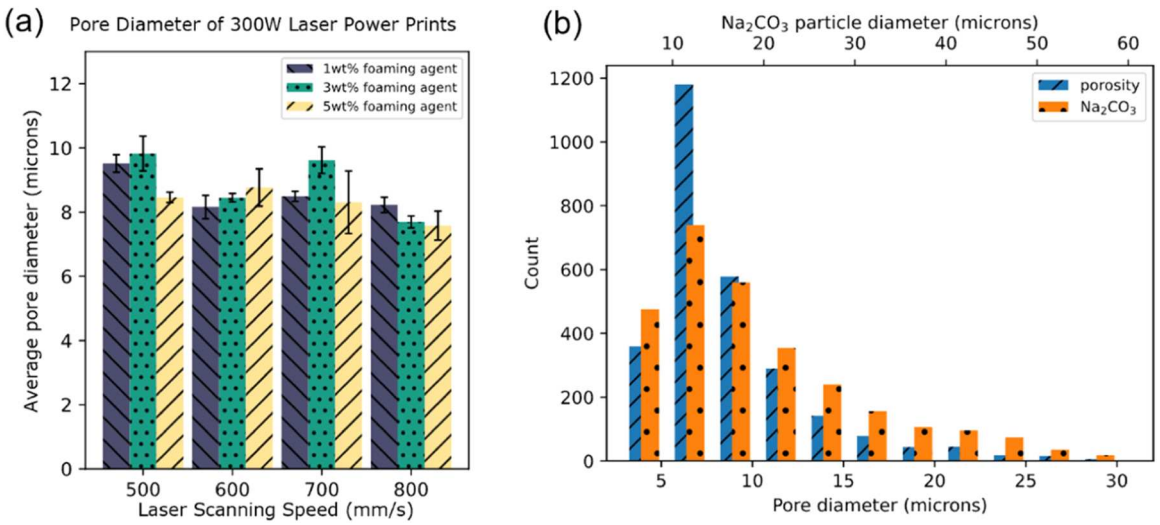

Fig. 7. (a) Final average pore diameter of experiments using various feedstock foaming agent content and various laser scanning speeds (constant 300 W laser power). (b) Combined pore size distribution in the final frame of all experiments with Na_2CO_3 foaming agent particle size plotted together.

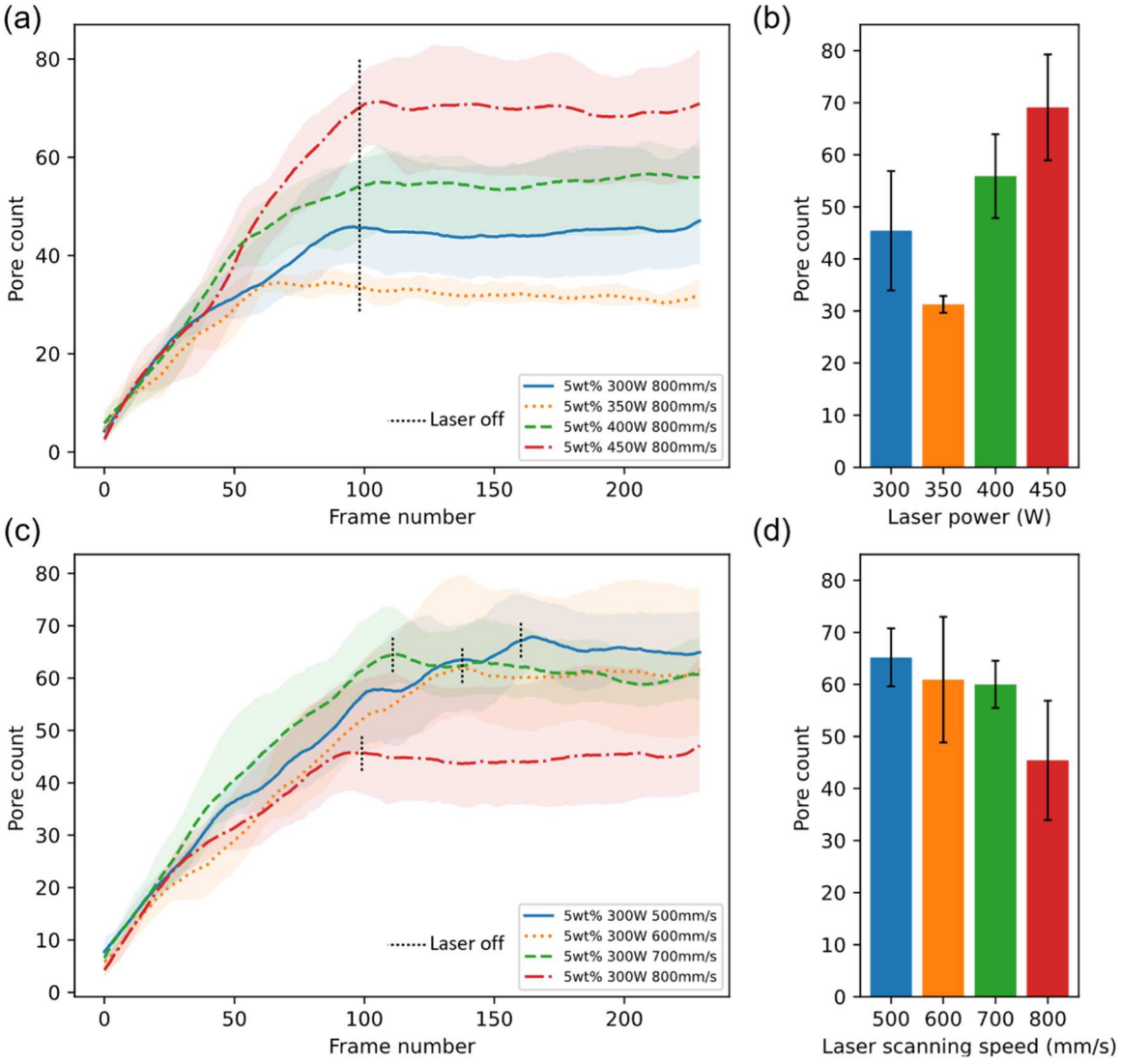

Fig. 8. Pore count results from experiments using 5 wt% Na_2CO_3 feedstock and single process condition variable: (a) Absolute pore count with respect to frame number and (b) Final absolute pore count of experiments using various laser powers. (c) Absolute pore count development with respect to frame number and (d) Final absolute pore count of experiments using various laser scanning speeds.

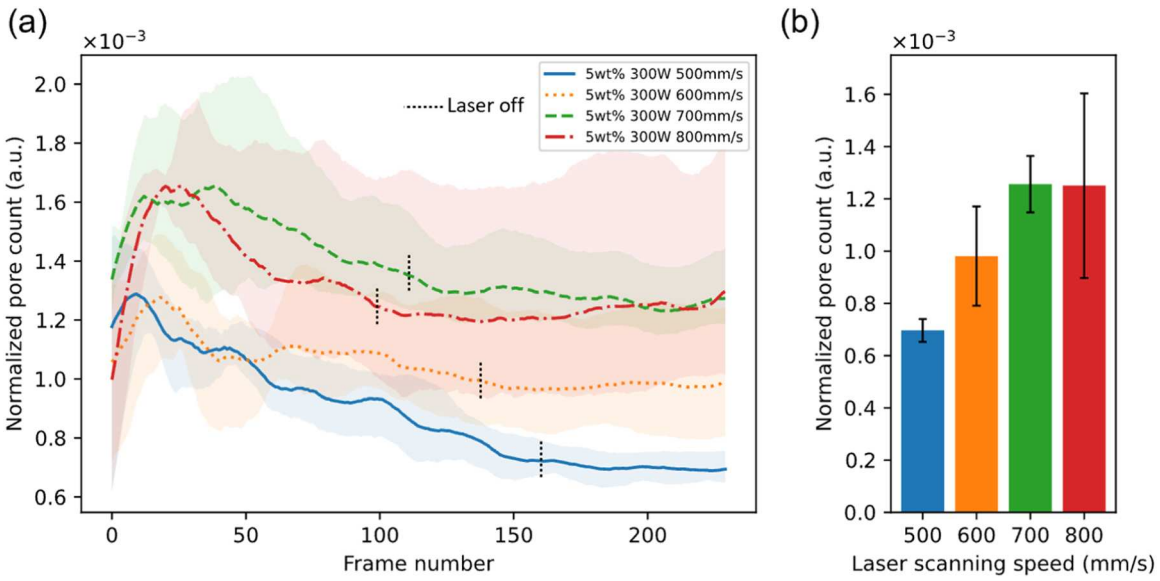

Fig. 9. (a) Normalized porosity count development with respect to frame number and (b) Final normalized porosity count of experiments using various laser scanning speeds.

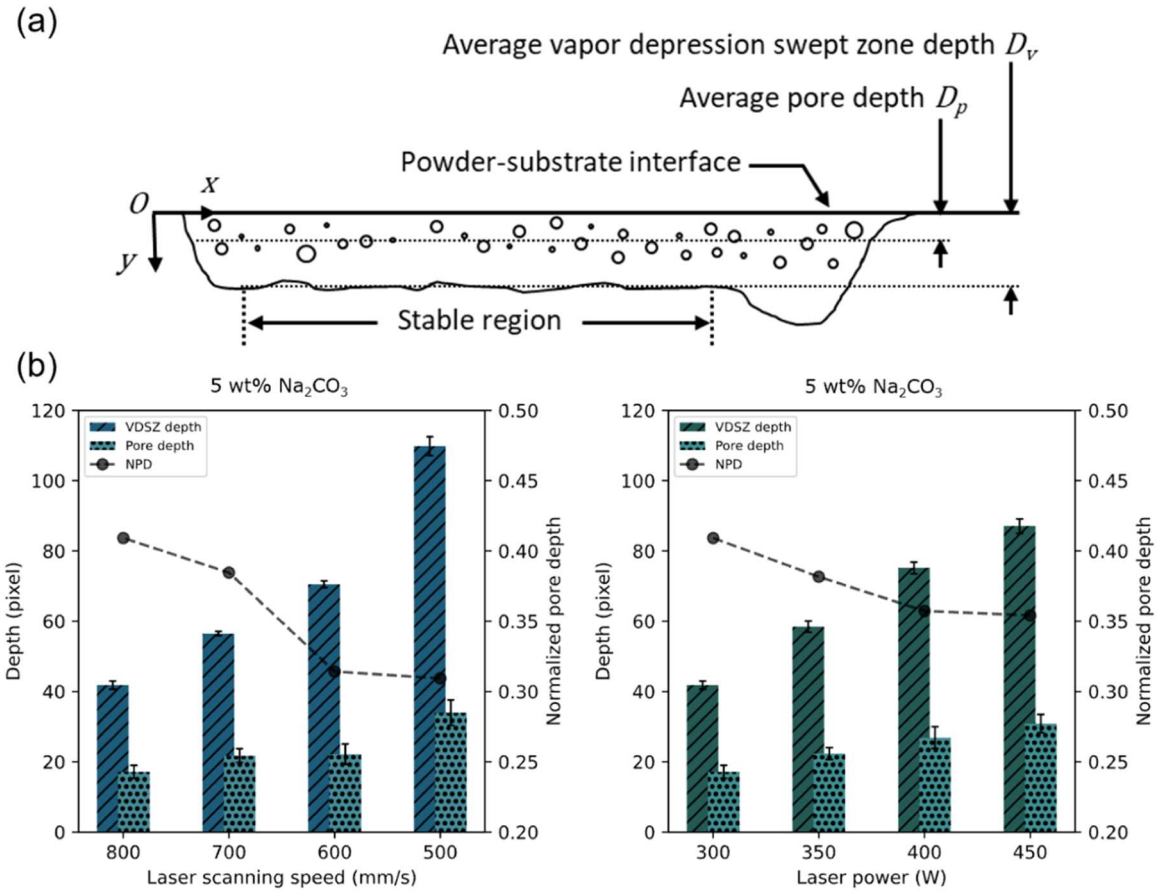

Fig. 10. (a) Illustration of the definition of various parameters used in the calculation of normalized pore depth (*NPD*). (b) Average vapor depression swept zone (VDSZ) depth, average pore depth, and normalized pore depth plot of experiments using 5 wt% Na_2CO_3, 300 W laser power, and various laser scanning speeds in reverse order (left); or 5 wt% Na_2CO_3, 800 mm/s laser scanning speed and various laser powers (right).

D_v, using which the normalized pore depth (*NPD*) is calculated as follows:

$$NPD = D_p / D_v$$

In a hypothetical print with pores well spread in the vertical direction, an *NPD* around 0.5 should be expected, and any deviation from the ideal value of 0.5 indicates a stabilized pore location bias in the vertical direction.

When the energy density of the laser source increases in the form of reduced scanning speed or increased power, the *NPD* reduces despite the increasing melt pool depth, as shown in Fig. 10(b). This indicates the reduced effectiveness of increasing melt pool depth to form pores at higher depths in the melt pool. And vice versa, increasing scanning speed (reducing energy density) is an effective strategy to improve the vertical spread of pores in a single track print. A similar trend was observed across various feedstock foaming agent content, as shown in Supplementary Figure 5. Therefore, increasing melt pool depth may not be an effective way to promote the uniform vertical spread of pores. However, it should be noted that the remelting of the previous layer, a basic feature of AM to achieve good interlayer bonding, could partially redistribute already-formed pores. Pores from the previous layer, especially those near the top, could be re-mobilized and enter the melt pool of the new layer from below. In addition, it has been shown in another L-PBF study that remelting of the previous layer in subsequent layer printing induces further decomposition of unreacted foaming agents in the previous layer [43]. This could also be beneficial to improve the vertical spread of pores in multi-layer prints since decomposition of unreacted foaming agents in the previous layer could be achieved.

The overall porosity level of a porous metal structure is another important metric for comparison. For completed parts or multi-layer prints, the overall porosity level is typically the ratio of the total volume of pores over the total exterior volume of the part/print. In a single-layer line scan, this could be equivalent to the fraction of the total 2D area of pores over the total 2D area of the vapor depression swept zone. However, this might not be a good approximation of a single layer's contribution to the porosity level of an overall part or a multi-layer print. A good interlayer bonding in AM relies on partial remelting of the previous layer during printing of the current layer, and the extent of previous layer remelting is dependent on the processing parameters used. For L-PBF processes with a constant layer height setting, the added exterior volume to the print is determined by the laser-scanned area within the current layer and the layer height. Therefore, normalizing the formed porosity volume by the added print volume is a better approximation of the single-layer foaming performance. A powder layer of 100 μm thickness is used in all systematic experiments with a line scan length of 1.6 mm. These two values are used to calculate the 2D equivalent of the added print volume, which was used to normalize the 2D equivalent of total porosity volume and deduce the porosity level of the single line scan. It is important to point out that the calculated porosity level is an underestimate of the actual porosity, as pores formed above the powder-substrate interface and those resulting from further decomposition of unreacted foaming agents during previous layer remelting are not considered.

One of the main goals of this systematic study is to understand if there is any relationship between the overall porosity level of the print and parameters involved in printing, such as laser power, scanning speed, and feedstock foaming agent content. The effect of altering laser power or scanning speed while holding the other parameter constant was studied using the feedstock with a 5 wt% foaming agent. As shown in Fig. 11(a), increasing the laser power has an overall positive impact on the porosity level, despite the slight decrease from 300 W, 800 mm/s runs to 350 W, 800 mm/s runs. Increasing the laser scanning speed reduces the energy density and causes an overall decrease in the porosity level despite the relatively large standard deviation, as shown in Fig. 11(b). Fig. 11(c) shows that experiments using 1 wt% foaming agent and 3 wt% foaming agent in feedstock also have a similar decreasing trend in porosity level with increasing laser scanning speed (decreasing energy density).

In addition to the similarity seen in the decreasing trend in porosity level with increasing laser scanning speed, the porosity levels themselves also show similarity across different feedstock foaming agent content, especially under high laser scanning speeds. Under the highest energy density condition (lowest laser scanning speed), the feedstock with the highest content of foaming agent (5 wt%) surprisingly produces the lowest porosity level, as shown in Fig. 11(c). This is against the intuition that a feedstock powder mix containing more foaming agents produces a higher porosity level when holding all processing parameters constant. This counterintuitive nature reveals an important consideration when choosing the foaming agents for AM. When considering the addition of foaming agent particles into feedstock powder, its interaction with the heat source is not to be overlooked. As shown in Supplementary Figure 6, the foaming agent used in the systematic study, pure Na_2CO_3 powder, has negative absorptivity against PTFE (a standard high reflectance reference material). In other words, Na_2CO_3 is almost a perfectly reflective material, making it nearly impossible to be heated directly by a laser, a common energy source used in AM. Also shown in Supplementary Figure 6 are the bulk powder absorptivity reduction caused by the introduction of reflective foaming agent powder into the feedstock. It can be reasonably hypothesized that when a large volume percentage of reflective foaming agent is mixed into the metal feedstock

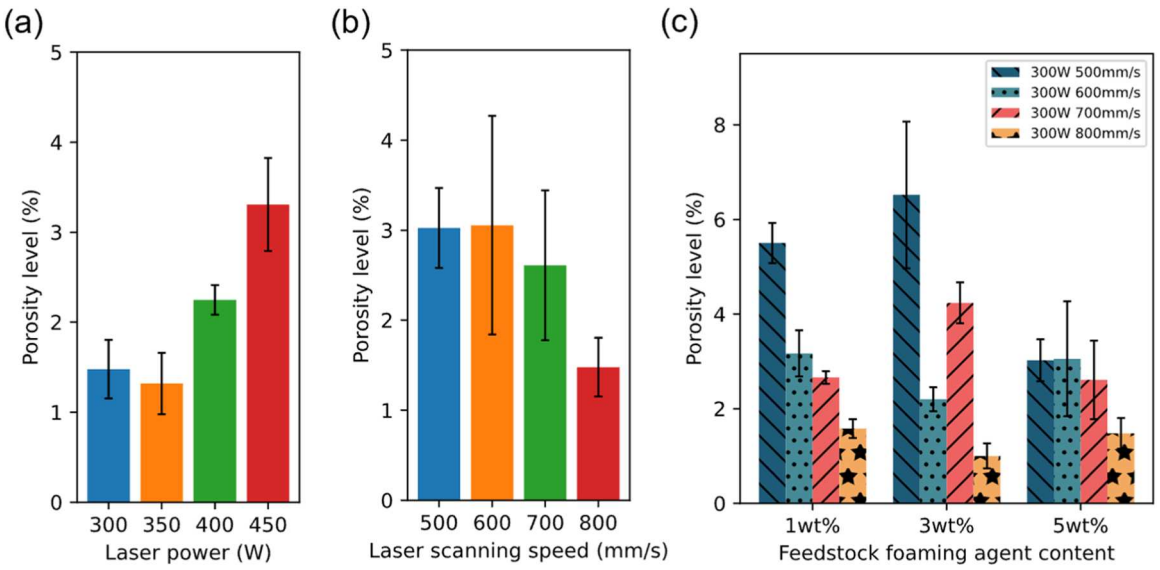

Fig. 11. (a) Final average porosity level of experiments using 5 wt% Na_2CO_3, 800 mm/s laser scanning speed, and various laser powers. (b) Final average porosity level of experiments using 5 wt% Na_2CO_3, 300 W laser power, and various laser scanning speeds. (c) Final average porosity level of experiments using various feedstock foaming agent content and various laser scanning speeds (constant 300 W laser power).

powder, the powder bed becomes more laser reflective. While it has not been shown to create a significant impact on processing conditions of Ti64 in the current study, the high laser reflectivity of Na_2CO_3 could contribute to a different heating mode of the foaming agent. In contrast to a more laser absorbing foaming agent, such as the TiH_2 used in the pilot study, it could be hypothesized that Na_2CO_3 foaming agent is being heated primarily through conduction from the surrounding molten metal instead of directly absorbing energy from the incident laser. The stark contrast in foaming performances using TiH_2 and Na_2CO_3 as shown in the pilot study could therefore be a combined result of the shift in foaming agent heating mode and the differences in decomposition temperature of the two foaming agents. For a more laser reflective foaming agent, such as Na_2CO_3, once its content within the feedstock goes beyond a certain threshold, it could present some challenges in achieving sufficient conductive heating from the peripheral molten metal, as shown in Fig. 12.

The estimated decomposition time of foaming agent particles at melt pool temperature is shown in **Supplementary Note 1** to be much less than the laser incident time. However, due to the aforementioned heating mechanism, high foaming agent laser reflectivity could hinder some of the foaming agent particles (in a high foaming agent content feedstock) from reaching decomposition activation temperature. Although the proposed shift in foaming agent heating and activation requires future experimental verifications, the results highlight the necessity of considering the impact of foaming agent laser absorptivity on expected overall porosity level.

4. Conclusion

In this work, in-situ high-speed imaging experiments of porous metal production using L-PBF were performed, and the never-seen-before dynamic development of porosities within the melt pool was revealed. Through a series of carefully designed experiments and control studies, the relationship between printing conditions (feedstock, laser power, and laser scanning speed) and the porosity properties of the print (pore size, count, depth, and overall porosity level) was systematically studied. The main conclusions from our study are summarized as follows:

(1) The average pore size in porous metal produced with L-PBF is largely dependent on the foaming agent particle size when pore coalescence is minimal. Similarly, without major pore coalescences, the feedstock foaming agent content, laser power, and laser scanning speed all show minimal to no impact on the average porosity size.

(2) For each of the feedstock foaming agent content tested, increasing laser power or reducing laser scanning speed causes an increase in the number of porosities formed, with laser power having a more significant influence.

(3) The idea of normalized pore depth is proposed to represent the average vertical spread of formed pores. Increasing the energy density in the form of increasing laser power or reducing scanning speed causes a reduction in pores' relative depth in the melt pool and consequently reduces the pore uniformity in the vertical direction.

(4) Increasing linear energy density in the form of increasing laser power or reducing laser scanning speed promotes the overall porosity addition of a single layer to multi-layer prints. However, it should be noted that decreasing scan speed may have a negative impact on the overall productivity of the L-PBF process and causes pore formation closer to the surface despite forming a deeper melt pool.

(5) Laser absorptivity and the kinetics of decomposition with respect to time scales of AM processing are important considerations for choosing a foaming agent in laser-based AM of porous metal. Foaming agent with low activation temperature and high decomposition rate can hinder pore retention during solidification in AM. In addition, foaming agents with low laser absorptivity may prevent direct heating by the laser and reduce the effectiveness of laser heating on the feedstock powder bed as a whole.

These exciting results encourage future investigations on the direct measurement of foaming agent laser interaction, foaming dynamics of multi-layer prints that include interlayer phenomenon, as well as comparison of foaming dynamics and dimensional accuracy against porous metal produced using other AM processes (such as DED). While the current study focuses on the Ti64/Na_2CO_3 material couple, we believe the results are reasonably applicable to other materials couples to improve the control of foaming outcomes, creating high-performance porous metal structures with intricate geometries only achievable via AM.

CRediT authorship contribution statement

Atieh Moridi: Writing – review & editing, Supervision, Funding acquisition, Conceptualization. **Kamel Fezzaa:** Writing – review & editing, Supervision, Investigation. **Samuel J. Clark:** Writing – review & editing, Supervision, Investigation. **Ashlee Gabourel:** Investigation.

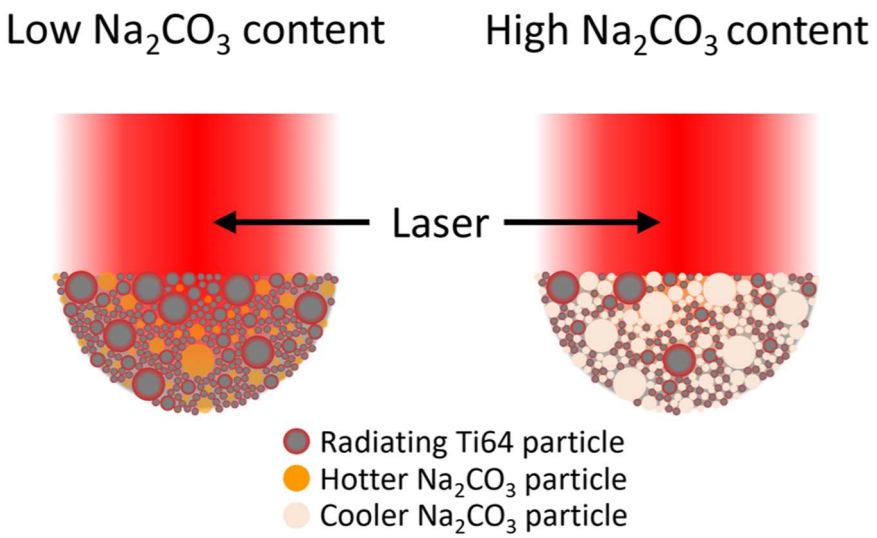

Fig. 12. Illustration of the effect of feedstock foaming agent overloading on thermal activation of foaming agent decomposition.

Akane Wakai: Writing – review & editing, Investigation. **Jenniffer Bustillos:** Methodology, Investigation. **Chenxi Tian:** Writing – original draft, Visualization, Validation, Software, Methodology, Investigation, Formal analysis.

Declaration of Competing Interest

The authors declare that they have no known competing financial interests or personal relationships that could have appeared to influence the work reported in this paper.

Acknowledgment

This research used resources of the Advanced Photon Source, a U.S. Department of Energy (DOE) Office of Science User Facility operated for the DOE Office of Science by Argonne National Laboratory under Contract [DE-AC02–06CH11357]. This work also made use of the Cornell Center of Materials Research Shared Facilities, which are supported through the NSF MRSEC program [DMR-1719875]. A.M. gratefully acknowledges the funding received by the National Science Foundation CAREER Award [CMMI-2046523] and the Office of Naval Research Young Investigator award [N00014–22–1–2420]. The authors acknowledge Sai Pratyush Akula for his assistance in performing partial experiments of the pilot study.

Appendix A. Supporting information

Supplementary data associated with this article can be found in the online version at doi:10.1016/j.addma.2024.104505.

Data availability

Data will be made available on request.

References

[1] L.P. Lefebvre, J. Banhart, D.C. Dunand, Porous metals and metallic foams: current status and recent developments, Adv. Eng. Mater. 10 (2008) 775–787, https://doi.org/10.1002/adem.200800241.
[2] Q. Han, C. Wang, H. Chen, X. Zhao, J. Wang, Porous tantalum and titanium in orthopedics: a review, ACS Biomater. Sci. Eng. 5 (2019) 5798–5824, https://doi.org/10.1021/acsbiomaterials.9b00493.
[3] P. Bai, X. Yang, X. Shen, X. Zhang, Z. Li, Q. Yin, G. Jiang, F. Yang, Sound absorption performance of the acoustic absorber fabricated by compression and microperforation of the porous metal, Mater. Des. 167 (2019), https://doi.org/10.1016/j.matdes.2019.107637.
[4] B. Zhu, M. Duke, L.F. Dumée, A. Merenda, E. des Ligneris, L. Kong, P.D. Hodgson, S. Gray, Short review on porous metal membranes—fabrication, commercial products, and applications, Membr. (Basel) 8 (2018), https://doi.org/10.3390/membranes8030083.
[5] H. Singh, P. Saxena, Y.M. Puri, The manufacturing and applications of the porous metal membranes: a critical review, CIRP J. Manuf. Sci. Technol. 33 (2021) 339–368, https://doi.org/10.1016/j.cirpj.2021.03.014.
[6] Q. Fang, J. Zhang, Y. Zhang, J. Liu, Z. Gong, Mesoscopic investigation of closed-cell aluminum foams on energy absorption capability under impact, Compos Struct. 124 (2015) 409–420, https://doi.org/10.1016/j.compstruct.2015.01.001.
[7] K.A. Dannemann, J. Lankford, High strain rate compression of closed-cell aluminium foams, 2000. ⟨www.elsevier.com/locate/msea⟩.
[8] J. Banhart, Aluminium foams for lighter vehicles, Int. J. Veh. Des. 37 (2005) 114, https://doi.org/10.1504/IJVD.2005.006640.
[9] M.F. Ashby, A. Evans, N.A. Fleck, L.J. Gibson, J.W. Hutchinson, H.N.G. Wadley, Metal foams: a design guide, Elsevier, 2000.
[10] J. Banhart, Manufacture, characterisation and application of cellular metals and metal foams, Prog. Mater. Sci. 46 (2001) 559–632, https://doi.org/10.1016/S0079-6425(00)00002-5.
[11] T. Miyoshi, M. Itoh, S. Akiyama, A. Kitahara, ALPORAS aluminum foam: Production process, properties, and applications, Adv. Eng. Mater. 2 (2000) 179–183, https://doi.org/10.1002/(SICI)1527-2648(200004)2:4<179::AID-ADEM179>3.0.CO;2-G.
[12] R. Jamshidi-Alashti, G. Roudini, Producing replicated open-cell aluminum foams by a novel method of melt squeezing procedure, Mater. Lett. 76 (2012) 233–236, https://doi.org/10.1016/j.matlet.2012.02.088.
[13] M. Thomas, D. Kenny, H. Sang, Particle-stabilized metal foam and its production, 5622542, 1997.
[14] H. Nakajima, Fabrication, properties and application of porous metals with directional pores, Prog. Mater. Sci. 52 (2007) 1091–1173, https://doi.org/10.1016/j.pmatsci.2006.09.001.
[15] T. Ikeda, H. Nakajima, T. Aoki, Fabrication of lotus-type porous stainless steel by continuous zone melting technique and mechanical property, Metall. Mater. Trans. A 36 (2005) 77–86, https://doi.org/10.1007/s11661-005-0140-1.
[16] H. Onishi, S.K. Hyun, H. Nakajima, Effect of hydrogen pressure on moisture-based fabrication of lotus-type porous nickel (in:), Mater. Trans. (2006) 2120–2124, https://doi.org/10.2320/matertrans.47.2120.
[17] P. Pinto, N. Peixinho, F. Silva, D. Soares, Compressive properties and energy absorption of aluminum foams with modified cellular geometry, J. Mater. Process Technol. 214 (2014) 571–577, https://doi.org/10.1016/j.jmatprotec.2013.11.011.
[18] C.-J. Yu, H.H. Eifert, J. Banhart, J. Baumeister, Metal foaming by a powder metallurgy method: production, properties and applications, Mater. Res. Innov. 2 (1998) 181–188, https://doi.org/10.1007/s100190050082.
[19] M.A. Atwater, L.N. Guevara, K.A. Darling, M.A. Tschopp, Solid state porous metal production: a review of the capabilities, characteristics, and challenges, Adv. Eng. Mater. 20 (2018), https://doi.org/10.1002/adem.201700766.
[20] D.P. Mondal, H. Jain, S. Das, A.K. Jha, Stainless steel foams made through powder metallurgy route using NH4HCO3 as space holder, Mater. Des. 88 (2015) 430–437, https://doi.org/10.1016/j.matdes.2015.09.020.
[21] T. DebRoy, H.L. Wei, J.S. Zuback, T. Mukherjee, J.W. Elmer, J.O. Milewski, A. M. Beese, A. Wilson-Heid, A. De, W. Zhang, Additive manufacturing of metallic components – process, structure and properties, Prog. Mater. Sci. 92 (2018) 112–224, https://doi.org/10.1016/j.pmatsci.2017.10.001.
[22] B. Levine, A new era in porous metals: Applications in orthopaedics, Adv. Eng. Mater. 10 (2008) 788–792, https://doi.org/10.1002/adem.200800215.
[23] X. Wang, S. Xu, S. Zhou, W. Xu, M. Leary, P. Choong, M. Qian, M. Brandt, Y.M. Xie, Topological design and additive manufacturing of porous metals for bone scaffolds and orthopaedic implants: a review, Biomaterials 83 (2016) 127–141, https://doi.org/10.1016/j.biomaterials.2016.01.012.
[24] B. Vamsi Krishna, W. Xue, S. Bose, A. Bandyopadhyay, Engineered porous metals for implants, JOM 60 (2008) 45–48, https://doi.org/10.1007/s11837-008-0059-2.
[25] S. Sanchez, A. Zafari, A.G. Demir, L. Caprio, B. Previtali, M. Holynska, I. Gibson, D. Jafari, Fine Porous Structures Fabricated Using Laser Powder Bed Fusion of Ti–6Al–4 V, in: I. Drstvensek, S. Pal, N. Ihan Hren (Eds.), Additive Manufacturing in Multidisciplinary Cooperation and Production, Springer International Publishing, Cham, 2024, pp. 133–143, https://doi.org/10.1007/978-3-031-37671-9_12.
[26] A. Zafari, K. Kiran, I. Gimenez-Garcia, K. Xia, I. Gibson, D. Jafari, Framework for additive manufacturing of porous Inconel 718 for electrochemical applications, Mater. Des. 237 (2024), https://doi.org/10.1016/j.matdes.2023.112606.
[27] D. Oropeza, T. Seager, S. Firdosy, J. Guerra, K. Billings, J.P. Jones, D.C. Hofmann, S. Roberts, Porosity control of copper-based alloys via powder bed fusion additive manufacturing for spacecraft applications, J. Porous Mater. (2024), https://doi.org/10.1007/s10934-023-01544-x.
[28] H.J. Kim, D.S. Shim, Characterization of the deposit-foaming of pure aluminum and Al-Mg-0.7Si alloys using directed energy deposition based on their metallurgical characteristics and compressive behaviors, Addit. Manuf. 59 (2022), https://doi.org/10.1016/j.addma.2022.103119.
[29] J.Y. Seo, K.Y. Lee, D.S. Shim, Effects of process parameters on properties of porous foams formed by laser-assisted melting of steel powder (AISI P21)/foaming agent (ZrH2) mixture, Opt. Laser Technol. 98 (2018) 326–338, https://doi.org/10.1016/j.optlastec.2017.08.008.
[30] D.S. Shim, J.Y. Seo, H.S. Yoon, K.Y. Lee, W.J. Oh, Additive manufacturing of porous metals using laser melting of Ti6Al4V powder with a foaming agent, Mater. Res Express 5 (2018), https://doi.org/10.1088/2053-1591/aad117.
[31] S. Ja-Ye, S. Do-Sik, Compressive behavior of porous materials fabricated by laser melting deposition using AlSi12 powder and foaming agent, Mater. Res Express 6 (2019), https://doi.org/10.1088/2053-1591/aafc5a.
[32] J. An, C. Chen, M. Zhang, Effect of CaCO3 content change on the production of closed-cell aluminum foam by selective laser melting, Opt. Laser Technol. 141 (2021), https://doi.org/10.1016/j.optlastec.2021.107097.
[33] H.J. Yun, D. Abolhasani, T.W. Hwang, T. Lee, J.H. Kim, Y.H. Moon, Fabrication of porous titanium parts by powder bed fusion of Ti-TiH2blended powder, J. Mater. Res. Technol. 9 (2020) 3026–3037, https://doi.org/10.1016/j.jmrt.2020.01.033.
[34] N.D. Parab, C. Zhao, R. Cunningham, L.I. Escano, K. Fezzaa, W. Everhart, A. D. Rollett, L. Chen, T. Sun, Ultrafast X-ray imaging of laser–metal additive manufacturing processes, J. Synchrotron Radiat. 25 (2018) 1467–1477, https://doi.org/10.1107/S1600577518009554.
[35] C. Zhao, K. Fezzaa, R.W. Cunningham, H. Wen, F. De Carlo, L. Chen, A.D. Rollett, T. Sun, Real-time monitoring of laser powder bed fusion process using high-speed X-ray imaging and diffraction, Sci. Rep. 7 (2017), https://doi.org/10.1038/s41598-017-03761-2.
[36] G. Bradski, The OpenCV Library, Dr. Dobb'S. J. Softw. Tools (2000).
[37] W. Wang, H. Garmestani, S.Y. Liang, Prediction of molten pool size and vapor depression depth in keyhole melting mode of laser powder bed fusion, Int. J. Adv. Manuf. Technol. 119 (2022) 6215–6223, https://doi.org/10.1007/s00170-021-08295-6.
[38] C. Zhao, K. Fezzaa, R.W. Cunningham, H. Wen, F. De Carlo, L. Chen, A.D. Rollett, T. Sun, Real-time monitoring of laser powder bed fusion process using high-speed X-ray imaging and diffraction, Sci. Rep. 7 (2017), https://doi.org/10.1038/s41598-017-03761-2.
[39] R. Cunningham, C. Zhao, N. Parab, C. Kantzos, J. Pauza, K. Fezzaa, T. Sun, A.D. Rollett, Keyhole threshold and morphology in laser melting revealed by ultrahigh-speed x-ray imaging, 2019. ⟨https://www.science.org⟩.

[40] B.J. Simonds, J. Tanner, A. Artusio-Glimpse, P.A. Williams, N. Parab, C. Zhao, T. Sun, The causal relationship between melt pool geometry and energy absorption measured in real time during laser-based manufacturing, Appl. Mater. Today 23 (2021), https://doi.org/10.1016/j.apmt.2021.101049.
[41] R. Kumar, H. Miyaoka, K. Shinzato, T. Ichikawa, Analysis of sodium generation by sodium oxide decomposition on corrosion resistance materials: a new approach towards sodium redox water-splitting cycle, RSC Adv. 11 (2021) 21017–21022, https://doi.org/10.1039/d1ra02671b.
[42] D.S. Shim, J.Y. Seo, H.S. Yoon, K.Y. Lee, W.J. Oh, Additive manufacturing of porous metals using laser melting of Ti6Al4V powder with a foaming agent, Mater. Res Express 5 (2018), https://doi.org/10.1088/2053-1591/aad117.
[43] H.J. Yun, D. Abolhasani, T.W. Hwang, T. Lee, J.H. Kim, Y.H. Moon, Fabrication of porous titanium parts by powder bed fusion of Ti-TiH2blended powder, J. Mater. Res. Technol. 9 (2020) 3026–3037, https://doi.org/10.1016/j.jmrt.2020.01.033.
[44] A. Kulshreshtha, S.K. Dhakad, Preparation of metal foam by different methods: A review, in: Mater Today Proc, Elsevier Ltd, 2019, pp. 1784–1790, https://doi.org/10.1016/j.matpr.2020.02.375.
[45] H. Ricardo, Z. Sandim, B. Vieira Morante, P.A. Suzuki, Kinetics of Thermal Decomposition of Titanium Hydride Powder Using in situ High-temperature X-ray Diffraction (HTXRD), 2005.
[46] A. Bisht, B. Gangil, V.K. Patel, Selection of blowing agent for metal foam production: a review, J. Met., Mater. Miner. 30 (2020) 1–10, https://doi.org/10.14456/jmmm.2020.1.
[47] A. Sola, A. Nouri, Microstructural porosity in additive manufacturing: the formation and detection of pores in metal parts fabricated by powder bed fusion, J. Adv. Manuf. Process 1 (2019), https://doi.org/10.1002/amp2.10021.
[48] A. Mostafaei, C. Zhao, Y. He, S. Reza Ghiaasiaan, B. Shi, S. Shao, N. Shamsaei, Z. Wu, N. Kouraytem, T. Sun, J. Pauza, J.V. Gordon, B. Webler, N.D. Parab, M. Asherloo, Q. Guo, L. Chen, A.D. Rollett, Defects and anomalies in powder bed fusion metal additive manufacturing, Curr. Opin. Solid State Mater. Sci. 26 (2022), https://doi.org/10.1016/j.cossms.2021.100974.
[49] J.H. Tan, W.L.E. Wong, K.W. Dalgarno, An overview of powder granulometry on feedstock and part performance in the selective laser melting process, Addit. Manuf. 18 (2017) 228–255, https://doi.org/10.1016/j.addma.2017.10.011.
[50] S. Vock, B. Klöden, A. Kirchner, T. Weißgärber, B. Kieback, Powders for powder bed fusion: a review, Prog. Addit. Manuf. 4 (2019) 383–397, https://doi.org/10.1007/s40964-019-00078-6.
[51] J. Bustillos, J. Kim, A. Moridi, Exploiting lack of fusion defects for microstructural engineering in additive manufacturing, Addit. Manuf. 48 (2021), https://doi.org/10.1016/j.addma.2021.102399.
[52] C. Zhao, N.D. Parab, X. Li, K. Fezzaa, W. Tan, A.D. Rollett, T. Sun, Critical instability at moving keyhole tip generates porosity in laser melting, Science 370 (1979) (2020) 1080–1086, https://doi.org/10.1126/science.abd1587.
[53] R. Cunningham, C. Zhao, N. Parab, C. Kantzos, J. Pauza, K. Fezzaa, T. Sun, A.D. Rollett, Keyhole threshold and morphology in laser melting revealed by ultrahigh-speed x-ray imaging, 2019. ⟨https://www.science.org⟩.
[54] Q. Guo, C. Zhao, M. Qu, L. Xiong, S.M.H. Hojjatzadeh, L.I. Escano, N.D. Parab, K. Fezzaa, T. Sun, L. Chen, In-situ full-field mapping of melt flow dynamics in laser metal additive manufacturing, Addit. Manuf. 31 (2020), https://doi.org/10.1016/j.addma.2019.100939.
[55] V. Kevorkijan, Low Cost Aluminum Foams Made by CaCO3 Particulates, 2010.